ACS OMEGA

Open Access



http://pubs.acs.org/journal/acsodf

Article

# Relationships between the Surface Hydrophilicity of a Bismuth Electrode and the Product Selectivity of Electrocatalytic $CO_2$ Reduction

Yujing Ji, Jichuang Wu, Ha Eun Lee, Yongsu An, Duk-Young Jung, Chan Woo Lee, Young Dok Kim,* and Hyun Ook Seo*

Cite This: *ACS Omega* 2024, 9, 48855−48866

Read Online

ACCESS | Metrics & More | Article Recommendations | Supporting Information

**ABSTRACT:** Two types of bismuth films (micro-Bi and nano-Bi) were prepared, and their electrocatalytic behavior was studied in terms of reduction current and product selectivity in a potential range of −0.776 to −1.376 V vs RHE. $CO_2$ and $H_2O$ molecules competed with each other for reduction on the surfaces of both types of films, and formate and $H_2$ were the respective major products of reductive reactions. Under the same conditions, nano-Bi exhibited lower selectivity for formate and higher selectivity for $H_2$ compared to the respective micro-Bi cases with bismuth films of similar thickness. This can be attributed to the higher hydrophilicity of bismuth film surfaces of nano-Bi due to surface nanoscale roughness and lower surface-carbon content compared with those of micro-Bi. Our results suggest a new strategy for controlling the selectivity of electrocatalytic $CO_2$ reduction under aqueous electrolytes through the use of surface engineering.

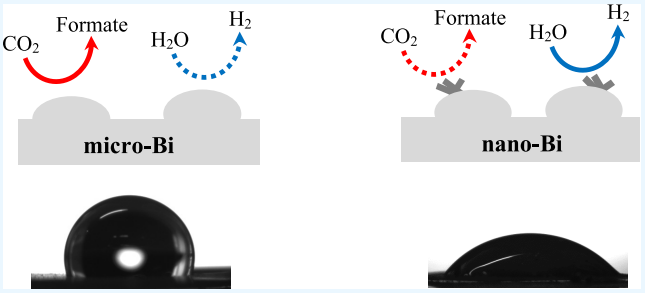


## 1. INTRODUCTION

Atmospheric $CO_2$ concentrations have increased since the beginning of the industrial revolution of the mid-18th century due to anthropogenic $CO_2$ emissions that have reached unprecedentedly high levels and are now causing serious environmental issues, such as global warming and sea level rise.[1−4] The combustion of fossil fuels is the primary source of anthropogenic $CO_2$ emissions drawing considerable attention to the development of renewable alternatives such as wind, solar, and tidal technologies.[5−8] Several different strategies, including chemical reforming,[9−12] biological,[13−15] and electrochemical[16−18] processes have been investigated to convert $CO_2$ into other carbon compounds that can be sequestered from the atmosphere.

Electrochemical $CO_2$ reduction has been considered a promising approach to addressing high concentrations of $CO_2$ due to the possibility of producing high-value chemicals from $CO_2$, e.g., $CO_2$-to-formate (formic acid) conversion powered by renewable energy. Formate is an important organic material used as a chemical feedstock in the pharmaceutical, pesticide, and chemical industries.[19−23] In addition, formate has the potential to serve as a hydrogen energy carrier due to its high volumetric hydrogen density, low toxicity, and low flammability under ambient air conditions.[24−26]

However, electrochemical $CO_2$ reduction suffers from sluggish kinetics, requiring high overpotentials. As electrochemical $CO_2$ reduction into formate also involves multiple electron and proton transfers, a variety of byproducts (e.g., CO, HCHO, $CH_3OH$, and $CH_4$) can be formed during the electrochemical reduction of $CO_2$.[27−30] Various electrocatalysts can lower the overpotential required for $CO_2$ reduction and increase product selectivity for formate. Pd, Cd, Hg, In, and Sn can reportedly catalyze the electrochemical $CO_2$ reduction into formate.[31−37] $CO_2$ reduction by a non-noble metal element, such as Ni, combined with a metal−organic framework has also been reported.[38,39]

Recently, bismuth has attracted great interest as an environmentally friendly and nontoxic metal catalyst for electrochemical $CO_2$ reduction as it exhibits high activity toward $CO_2$ reduction and high selectivity for conversion of $CO_2$ to formate.[40−44] Various bismuth-based electrocatalysts have been applied to the electrochemical conversion of $CO_2$ to formate.[40,45−50] Recent research has revealed links between the electrocatalytic performance of bismuth-based materials and their surface structures. For example, studies on $CO_2$ reduction using cobalt-doped bismuth nanosheet,[51] $Bi_2O_2CO_3$ nanosheets,[52] bismuthene,[53−55] and bismuth nano flowers[40] have demonstrated reduced overpotential for $CO_2$ reduction by

Received: October 23, 2024
Revised: November 10, 2024
Accepted: November 18, 2024
Published: November 26, 2024

bismuth-based electrocatalysts. Additionally, density functional theory (DFT) calculations suggested that the $Bi_2O_3$ nanocluster deposited on the other semiconducting materials (e.g., $TiO_2$) can activate adsorbed $CO_2$, facilitating $CO_2$ conversion.[56] The fast synthesis of bismuth-nanocatalysts, such as nanofoams and particles, via ultrafast thermal heating methods has also been demonstrated.[57,58] However, a deeper understanding of the relationships between surface structures and electrocatalytic performance is still required to design more efficient electrocatalysts for $CO_2$ reduction.

In the present work, we explored the relationships between bismuth surface affinity for water molecules and its electrocatalytic performance in the electrochemical reduction of $CO_2$ into formate under aqueous conditions. To achieve feasible and environmentally friendly electrocatalytic conversion of $CO_2$ into formate, it is necessary to operate the process under aqueous conditions, minimizing the use of organic solvents. However, under aqueous conditions, water reduction via the hydrogen evolution reaction (HER) inevitably competes with $CO_2$ reduction due to the similar standard reduction potentials of both reactions. Hydrogen gas is typically the major byproduct during electrocatalytic reduction of $CO_2$ to formate under aqueous conditions, making it crucial to minimize the HER throughout the process. In this study, we demonstrated that the formate selectivity in electrocatalytic $CO_2$ reduction over $H_2$ selectivity can be improved by reducing the surface affinity for water molecules (surface hydrophilicity) by controlling the surface roughness and carbon content.

## 2. RESULTS AND DISCUSSION

**2.1. Bismuth Films Consisted of Submicrometer Granules (Micro-Bi-180s, micro-Bi-300s, and micro-Bi-1800s).** *2.1.1. Characterization of Micro-Bi Samples (SEM and XRD).* Bismuth films consisting of submicrometer granules were prepared by electrodepositing bismuth on Cu foils. Three bismuth films were prepared by 180, 300, and 1800 s of bismuth electrodeposition, and they were named micro-Bi-180s, micro-Bi-300s, and micro-Bi-1800s, respectively. Figure 1a,b,c is topological scanning electron microscopy (SEM) images of micro-Bi-180s, micro-Bi-300s, and micro-Bi-1800s samples. The surfaces of the micro-Bi-180s and micro-Bi-300s samples consisted of irregularly shaped granular particles with diameters ranging from 400 to 800 nm. Similar to micro-Bi-180s and micro-Bi-300s samples, granular particles were found on the surface of the micro-Bi-1800s but those particles were larger than the particles on the other two samples.

The micro-Bi-180s, micro-Bi-300s, and micro-Bi-1800s samples were bisected using a sharp blade, and their cross-sectional SEM images were obtained (Figure 1d,e,f). Bismuth film approximately 10 $\mu$m thick formed after 180 s of electrodeposition of bismuth (micro-Bi-180s) (Figure 1d), whereas the thickness of the bismuth films increased to approximately 20 $\mu$m when the electrodeposition time was 300 s (micro-Bi-300s) (Figure 1e). However, when the electrodeposition time was further extended to 1800 s, the increase in film thickness was not significant (Figure 1f). It indicated that beyond a certain electrodeposition time, the deposited bismuth did not contribute an increase of film thickness. Instead, the bismuth began to deposit onto existing submicroparticles (400−800 nm in size) rather than forming new particles. It resulted in the enlargement of the existing bismuth particles and an increase in density of the film, but not in its thickness.

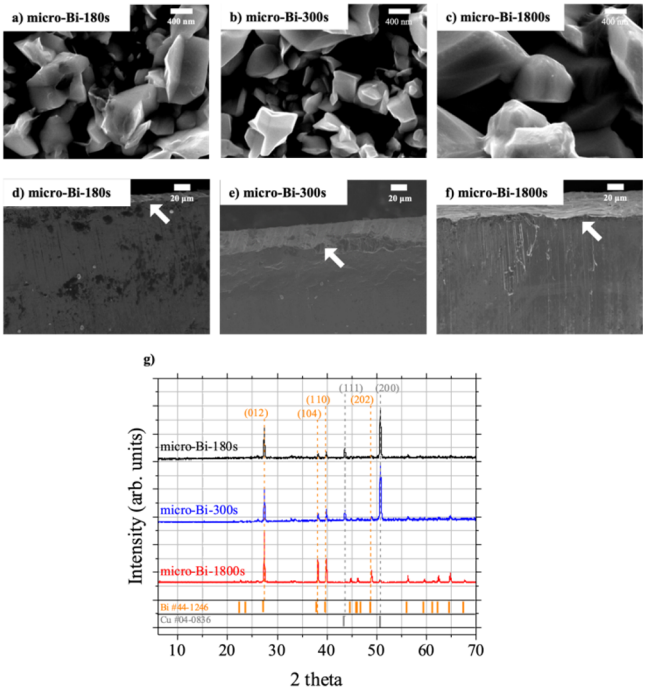


**Figure 1.** Characterization results of micro-Bi-180s, micro-Bi-300s, and micro-Bi-1800s. Topological SEM images of (a) micro-Bi-180s, (b) micro-Bi-300s, and (c) micro-Bi-1800s and cross-sectional SEM images of (d) micro-Bi-180s, (e) micro-Bi-300s, and (f) micro-Bi-1800s. (g) XRD patterns of micro-Bi-180s, micro-Bi-300s, and micro-Bi-1800s.

Additionally, energy-dispersive X-ray spectroscopy (EDS)-mapping analysis was conducted on the cross sections of three micro-Bi samples (Figure S1). For the case of micro-Bi-180s, the Bi atoms were distributed over the top surface layer with a thickness of 10 $\mu$m, where Cu-related signals were scarcely observed. Cu signals were detected beneath the top layer, indicating that the topmost surface of the micro-Bi-180s sample was predominantly composed of Bi atoms. Similarly, EDS-mapping images of the other two micro-Bi samples also confirmed that their top layers mainly consisted of Bi atoms with a negligible contribution from Cu atoms (Figure S1).

Figure 1g depicts the X-ray diffraction (XRD) patterns of the three micro-Bi samples. XRD peaks corresponding to bismuth crystalline planes were observed for all three samples (Figure 1g). Micro-Bi-180s and micro-Bi-300s samples exhibited similar XRD patterns, showing bismuth crystalline XRD peaks together with copper-related XRD peaks. However, very little copper-related peaks were observed for the case of the micro-Bi-1800s sample, which was accompanied by an increase of birelated XRD peak intensity. This can be attributed to the formation of films consisting of densely packed Bi atoms thicker than the penetration depth of X-ray (approximately 19.7 $\mu$m) under the XRD analysis conditions (S3).

*2.1.2. Electrocatalytic $CO_2$ Reduction (LSV Measurements under $N_2$ and $CO_2$ Flow).* The electrocatalytic behavior of the three micro-Bi samples toward $CO_2$ reduction was studied by measuring linear sweep voltammetry (LSV) curves under $N_2$ and $CO_2$ saturation (Figure S2). During LSV measurements, the potential applied to the micro-Bi samples decreased from −0.17 to −1.37 V vs RHE and currents between the micro-Bi sample and platinum counter-electrode were measured. For all


https://doi.org/10.1021/acsomega.4c09642
ACS Omega 2024, 9, 48855−48866

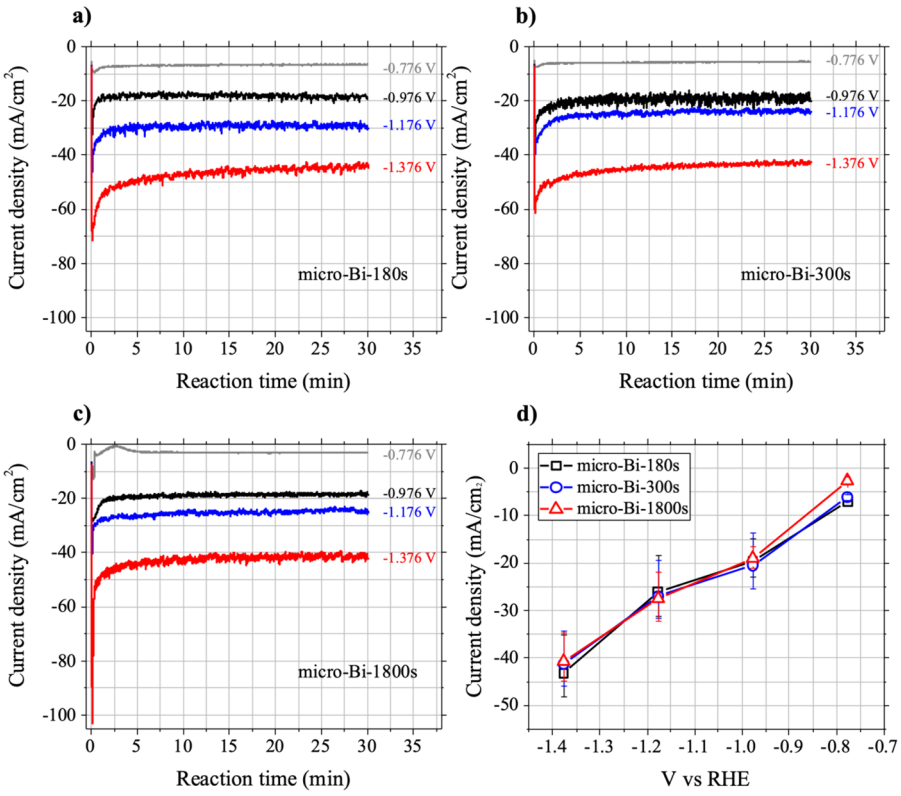


**Figure 2.** The results of chronoamperometry measurements. The results of chronoamperometry measurements at four different potential biases (−0.776, −0.976, −1.176, and −1.376 V vs RHE) with (a) micro-Bi-180s, (b) micro-Bi-300s, and (c) micro-Bi-1800s under $CO_2$ flow conditions. (d) Average current values of micro-Bi-180s, micro-Bi-300s, and micro-Bi-1800s.

three micro-Bi samples, a reduction current began to flow under $N_2$ when the applied potential on the sample was lower than approximately −0.6 V (vs RHE). The magnitude of the reduction current increased as micro-Bi was biased more negatively under the $N_2$ flow condition.

When the same LSV measurements were performed with three micro-Bi samples under a $CO_2$ flow, higher reduction currents were measured under the same potential bias conditions compared with the respective $N_2$ flow cases (Figure S2). The reduction currents measured under $N_2$ flow were attributable primarily to the reduction of water molecules to $H_2$ on the surface of the micro-Bi, whereas $CO_2$ reduction as well as water reduction contributed to the reduction currents measured under $CO_2$ flow. These results indicate that all three micro-Bi samples were electrocatalytically active toward $CO_2$ reduction under our experimental conditions.

*2.1.3. Electrocatalytic $CO_2$ Reduction (Chronoamperometry under $CO_2$ Flow).* The three micro-Bi samples produced similar LSV curves under both $N_2$ and $CO_2$ flow (Figure S2). To compare the electrocatalytic behavior of the three micro-Bi samples toward $CO_2$ reduction, chronoamperometry measurements were taken at four different potential biases (−0.776, −0.976, −1.176, and −1.376 V vs RHE) under $CO_2$ flow (Figure 2). For all three micro-Bi samples at the four different potential bias conditions, the magnitude of the reduction current increased rapidly as soon as the negative potentials were applied to the samples. The current density value spiked to its maximum magnitude in approximately 10 s, and then the current density magnitude decreased to its saturated values within 5 min. The spike in the magnitude of the current density at the earliest stage of the reaction can be attributed to the reduction of bismuth oxides, which were likely to form on the surface of micro-Bi samples upon exposure to ambient air before the chronoamperometry experiments. However, the saturated reduction current value (>approximately 5 min) for each case can be attributed largely to the reduction of $CO_2$ and water molecules on the surface of the micro-Bi samples where no more significant reduction of electrode surface took place.

The electrocatalytic behavior of the three micro-Bi samples under the four different bias conditions was then compared in terms of their saturated reduction current values (Figure 2d). Each value was obtained by averaging the current density over the datum from 5 to 30 min at the respective conditions. Each measurement was performed twice to obtain the average, minimum, and maximum values of the saturated reduction current (Figure 2d). The magnitude of the current gradually increased as more negative potential was applied to the bismuth film in all three micro-Bi samples due to the facilitation of reductive reactions of $CO_2$ and water on the surface of the bismuth films. However, three micro-Bi samples did not exhibit noticeably different behaviors in terms of current density at the same potential bias (Figure 2d).

*2.1.4. Electrocatalytic $CO_2$ Reduction (Product Analysis).* Various molecules, such as CO, $CH_4$, and formate, can be produced by electrochemical reduction of $CO_2$. Hydrogen gas can also be produced by reduction of water during electrochemical $CO_2$ reduction under aqueous conditions. After 30 min of each chronoamperometry experiment under a $CO_2$ flow, the products in both gas and liquid phases were analyzed by means of online gas chromatography (GC) and nuclear magnetic resonance (NMR), respectively. The formation of four different molecules ($CH_4$, CO, $H_2$, and formate) by


https://doi.org/10.1021/acsomega.4c09642
ACS Omega 2024, 9, 48855−48866

electrocatalytic $CO_2$ reduction in the presence of micro-Bi samples was confirmed by the analysis of the products. No C2 species such as $C_2H_6$ and $C_2H_4$ were detected after electrocatalytic reduction of $CO_2$ in any of the cases in this study. The amount of each product molecule generated after the $CO_2$ reduction experiment varied across the micro-Bi samples (micro-Bi-180s, micro-Bi-300s, and micro-Bi-1800s) and potential bias of the micro-Bi samples (−0.776, −0.976, −1.176, and −1.376 V vs RHE). Faraday efficiency (FE%) for each product molecule was calculated as follows:

$$\text{FE\%} = \frac{\text{no. of electrons consumed to form product molecules}}{\text{no. of electrons flowed}} \times 100\%$$

This can be expressed as follows,

$$\text{FE\%} = \frac{n_{\text{product}} \times Z \times F}{Q} \times 100\%$$

where $n_{\text{product}}$ is the number of produced molecules (formate, $CH_4$, CO, and $H_2$), and $Z$ is the number of electrons required to form a particular product molecule. $F$ is the Faraday constant (96485.3321 C/mol), while $Q$ is the number of electrons that flowed during the $CO_2$ reduction determined from current values during the reaction. Detailed information on the FE% calculation can be found in S5.

Table 1 summarizes the average FE% values for the four product molecules (formate, $CH_4$, CO, and $H_2$) obtained from two separate sets of experiments under the same conditions. Formate was the major product for which the FE% was greater than those of the other three products ($CH_4$, CO, and $H_2$) under all experimental conditions (Table 1 and Figure 3).

**Table 1. Summary of Faradaic Efficiency (FE%) Values of Micro-Bi-180s, Micro-Bi-300s, and Micro-Bi-1800s.**[a]

| micro-Bi-180s | | | | |
|---|---|---|---|---|
| V vs RHE | FE% for formate | FE% for $CH_4$ | FE% for CO | FE% for $H_2$ |
| −0.776 | 93.55 | 0 | 0.72 | 4.5 |
| −0.976 | 92.95 | 0 | 2.82 | 1.85 |
| −1.176 | 82.28 | 0.88 | 2.22 | 16.91 |
| −1.376 | 71.71 | 0.44 | 0.89 | 29.27 |
| micro-Bi-300s | | | | |
| V vs RHE | FE% for formate | FE% for $CH_4$ | FE% for CO | FE% for $H_2$ |
| −0.776 | 93.38 | 0 | 2.16 | 6.26 |
| −0.976 | 92.69 | 0.49 | 2.5 | 7.09 |
| −1.176 | 75.77 | 0.97 | 1.395 | 23.465 |
| −1.376 | 49.67 | 0.48 | 0.785 | 52.84 |
| micro-Bi-1800s | | | | |
| V vs RHE | FE% for formate | FE% for $CH_4$ | FE% for CO | FE% for $H_2$ |
| −0.776 | 84.07 | 0 | 2.32 | 10.90 |
| −0.976 | 94.46 | 0 | 3.06 | 5.13 |
| −1.176 | 85.48 | 0.64 | 1.96 | 13.65 |
| −1.376 | 61.21 | 0.69 | 1.21 | 38.20 |

[a]Summary of Faradaic efficiency (FE%) values for formate, $CH_4$, CO, and $H_2$ with micro-Bi-180s, micro-Bi-300s, and micro-Bi-1800s determined by 30 min of chronoamperometry under a constant $CO_2$ flow at four different potential biases (−0.776, −0.976, −1.176, and −1.376 V vs. RHE)

For the micro-Bi-180s and micro-Bi-300s samples, the FE% for formate gradually decreased as they were biased at more negative potentials, and this was accompanied by an increase in the FE% of $H_2$ (Table 1 and Figure 3). This implies the competition between water and $CO_2$ reductions on the surface of the bismuth films and the facilitation of water reduction over $CO_2$ reduction as the applied potentials became more negative. General trends of formate and $H_2$ FE% changes of the micro-Bi-1800s sample upon the biasing conditions were similar to the other two cases (micro-Bi-180s and micro-Bi-300s). The FE% formate increase (decrease) was always accompanied by a decrease (increase) of FE% for $H_2$, as did the micro-Bi-180s and micro-Bi-300s samples, indicating that water and $CO_2$ reductions competed with each other also on the surface of bismuth films of the micro-Bi-1800s. Among the three micro-Bi samples, the micro-Bi-180s sample was the least sensitive to the potential bias in terms of the FE% for formate, exhibiting the highest FE% for formate over the whole potential range (−0.776 to −1.376 V vs RHE) studied. It is worth to mention that the formate FE% of micro-Bi-1800s increased as the potential bias decreased from −0.776 to −0.976 V vs RHE unlike the other two cases (micro-Bi-180s and micro-Bi-300s). It was likely due to the larger particle size and denser film structure of the micro-Bi-1800s than the other two samples (micro-Bi-180s and micro-Bi-300s). This ensures further investigations in future research, which will also include studies on thinner bismuth films. However, such studies fall outside the main scope of this study. The primary focus of this study is on how the hydrophilicity of bismuth films influences their electrocatalytic behaviors, which will be discussed in detail in the following sections.

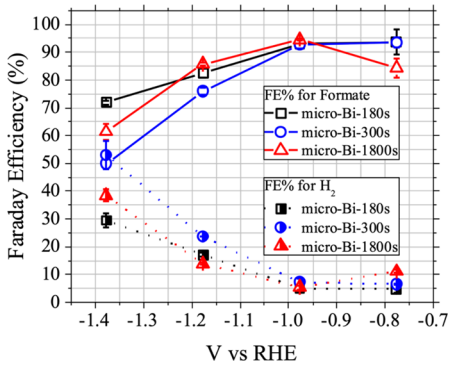


**Figure 3.** Comparison of Faradaic efficiency (FE%) values. Comparison of Faradaic efficiency (FE%) values for formate and $H_2$ with three micro-Bi samples (micro-Bi-180s, micro-Bi-300s, and micro-Bi-1800s) as determined by 30 min of chronoamperometry under a constant $CO_2$ flow at four different potential bias conditions (−0.776, −0.976, −1.176, and −1.376 V vs RHE).

**2.2. Nanostructured Bismuth Films (Nano-Bi-180s and Nano-Bi-300s).** Bismuth films composed of submicrogranules decorated with nanostructures were prepared by electrodepositing bismuth on electroless plated copper films on titanium foil. Two nanostructured bismuth films were prepared by 180 and 300 s of bismuth electrodeposition, and they were named nano-Bi-180s and nano-Bi-300s, respectively. With these two samples, the influence of hydrophilicity of bismuth films on their electrocatalytic behaviors toward $CO_2$ reduction was investigated.

The thicknesses of the bismuth films of the nano-Bi-180s and nano-Bi-300s samples were similar to those of the respective micro-Bi samples (Figure 4c,d). In addition, EDS-mapping analysis revealed that the top layers were mainly composed of Bi atoms with negligible contribution from Cu and Ti atoms similar to the micro-Bi samples (Figure S3).


https://doi.org/10.1021/acsomega.4c09642
ACS Omega 2024, 9, 48855−48866

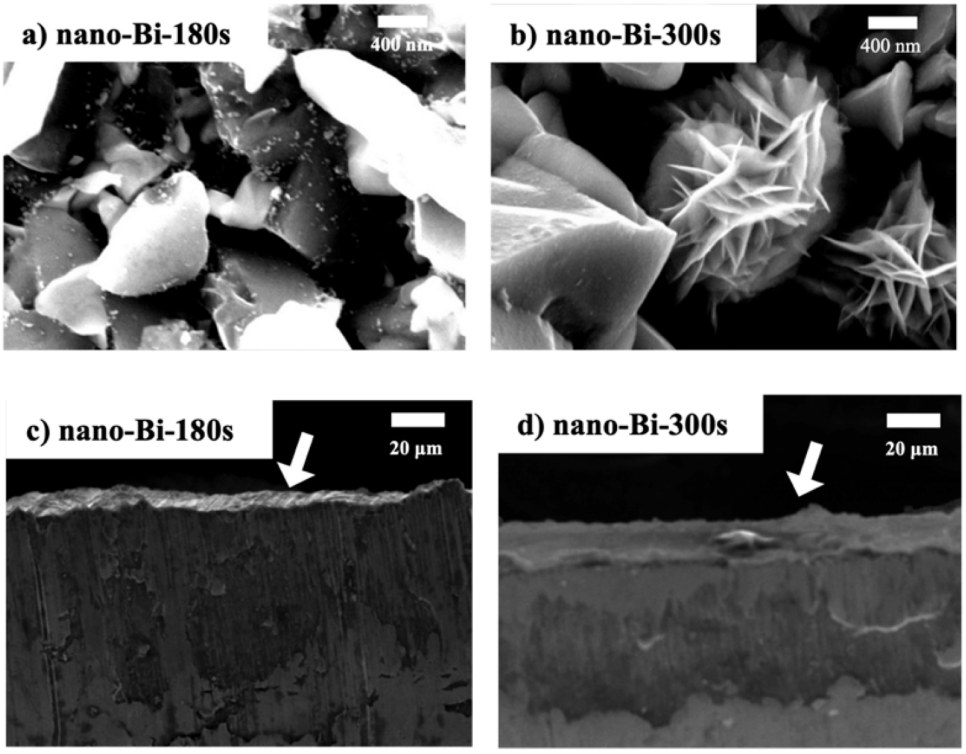


**Figure 4.** SEM images of nano-Bi-180s and nano-Bi-300s. Topological SEM images of (a) nano-Bi-180s and (b) nano-Bi-300s and cross-sectional SEM images of (c) nano-Bi-180s and (d) nano-Bi-300s.

However, additional nanostructures were evident on the surface of the bismuth films on the nano-Bi samples (Figure 4a,b). The surface of the nano-Bi-180s sample consisted of granular particles (400−800 nm in diameter) decorated with smaller nanoparticles, each a few tens of nanometers in diameter (Figure 4a). Additional flower-like plates, a few tens of nanometers thin, were found on the surface of the nano-Bi-300s sample together with granular particles (400−800 nm in diameter) (Figure 4b).

The electrocatalytic activity of the nano-Bi-180s and nano-Bi-300s samples toward $CO_2$ reduction in aqueous conditions was examined by measuring LSV curves under $N_2$ and $CO_2$ flow. Similar to the micro-Bi-180s and nano-Bi-300s samples, reduction current flowed when the reduction potentials applied to the bismuth films were less than approximately −0.6 V (vs RHE) and a reduction current with a greater magnitude flowed as more negative potentials were applied to the bismuth films of the nano-Bi-180s and nano-Bi-300s samples (Figure S4). The magnitude of the reduction in current measured under $CO_2$ flow was larger than those under $N_2$ flow for the nano-Bi-180s and nano-Bi-300s samples (Figure S4). This indicates that both nano-Bi samples were electrocatalytically active toward the reduction of $CO_2$ under our experimental conditions.

Chronoamperometry experiments were also performed with two nano-Bi samples under $CO_2$ flow at four different potential bias conditions (−0.776, −0.976, −1.176, and −1.376 V vs RHE), and the results are compared with those of the respective micro-Bi samples (micro-Bi-180s and nano-Bi-300s) in Figure 5a,b. A higher reduction current was measured for the nano-Bi-300s at −1.376 V (vs RHE) compared with that of micro-Bi-300s (Figure 5b). However, the behavior of the nano-Bi-180s and nano-Bi-300s samples with additional nanostructures (tens of nanometers in diameter) was otherwise almost identical to the respective micro-Bi samples, which consisted of granular particles (400−800 nm) without nanostructures of a few tens of nanometers in size (Figure 5a,b).

After 30 min of each chronoamperometry experiment, products of both the gas and liquid phases were analyzed by online GC and NMR. The formation of formate, $CH_4$, CO, and $H_2$ upon electrocatalytic $CO_2$ reduction with the two nano-Bi samples under our experimental conditions was revealed by a products analysis. The FE% for each product molecule was calculated as described in section 2.1.4. Table 2 summarizes the average FE% values for formate, $CH_4$, CO, and $H_2$ measured with nano-Bi-180s and nano-Bi-300s at four different potential bias conditions. Formate and $H_2$ were the primary products of electrocatalytic $CO_2$ reduction for the cases of two nano-Bi samples, similar to the behavior observed in the micro-Bi samples. The FE% values for formate and $H_2$ exhibited significant variations depending on the bias conditions (Table 2).

Formate and $H_2$ FE% values for the nano-Bi-180s and nano-Bi-300s were compared with those of the respective micro-Bi samples (micro-Bi-180s and micro-Bi-300s) (Figure 5c,d,e,f). The general trend in FE% changes for the nano-Bi samples upon decreasing the applied potential was similar to that of the corresponding micro-Bi samples. The formate FE% decreased with more negative applied potentials from −0.776 to −1.376 V (vs RHE), accompanied by an increase in $H_2$ FE%. This indicates that the $CO_2$ reduction on the nano-Bi samples also competed with water reduction, and water reduction was facilitated rather than the $CO_2$ reduction as the bismuth films were biased at more negative potentials (Figure 5c,d,e,f). Although general trends in the formate and $H_2$ FE% changes according to the bias conditions were similar between the nano-Bi and micro-Bi with similar bismuth film thicknesses, the nano-Bi samples exhibited lower formate FE and higher $H_2$


https://doi.org/10.1021/acsomega.4c09642
ACS Omega 2024, 9, 48855−48866

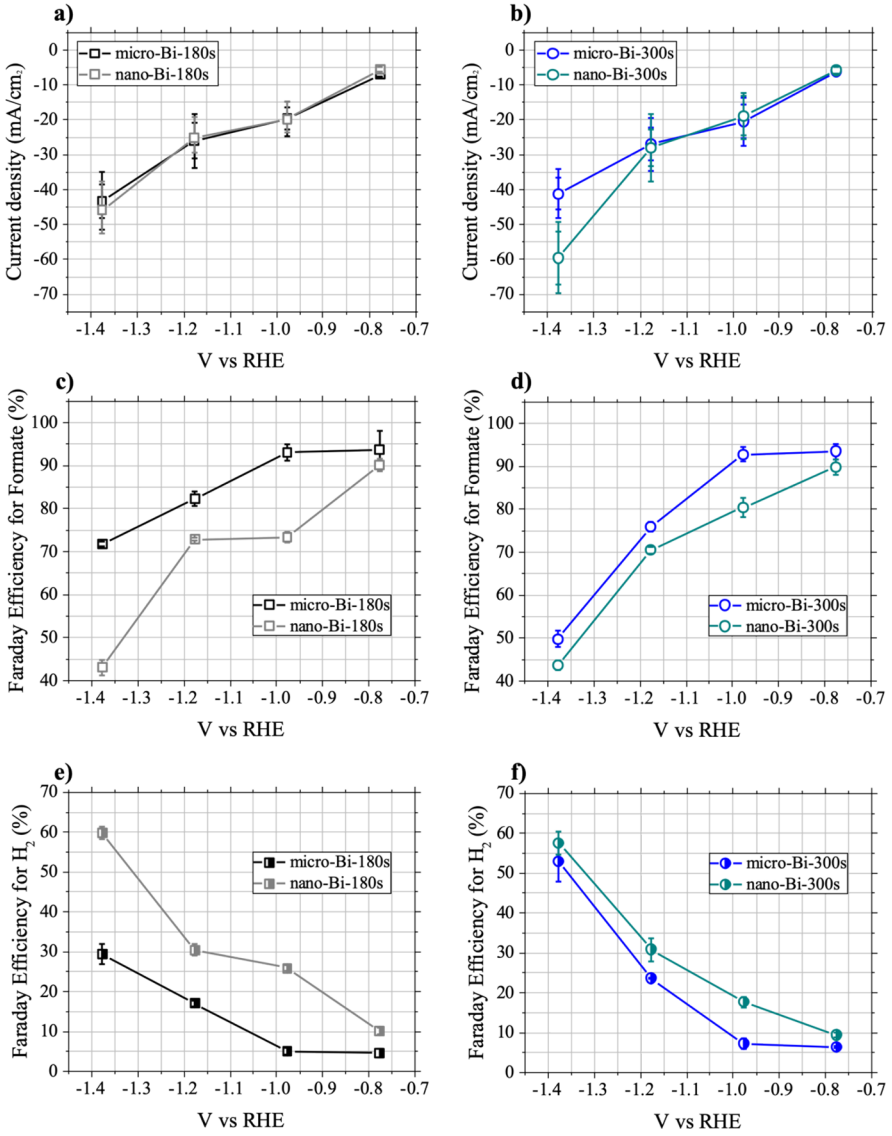


**Figure 5.** Comparison of micro- and nano-Bi samples (average current values, formate, and $H_2$FE% values). Average current values of (a) micro-Bi-180s and nano-Bi-180s and (b) micro-Bi-300s and nano-Bi-300s. Average Faradaic efficiency (FE%) values for formate of (c) micro-Bi-180s and nano-Bi-180s and (d) micro-Bi-300s and nano-Bi-300s. Average Faradaic efficiency (FE%) values for $H_2$ of (e) micro-Bi-180s and nano-Bi-180s and (f) micro-Bi-300s and nano-Bi-300s.

FE% compared to the respective micro-Bi sample at the same potential bias. In other words, the surface of bismuth films with additional nanostructures (nano-bi) exhibited greater propensity for water reduction during electrocatalytic reduction of $CO_2$ under aqueous conditions compared with the surface of bismuth films without nanostructures (micro-Bi) under the same experimental conditions.

**2.3. Further Analysis (Surface Hydrophilicity and XPS Analysis).** It was possible that additional nanostructures (a few tens of nanometers in diameter) on the surfaces of the nano-Bi samples increased the surface affinity toward water molecules compared with micro-Bi samples.[59,60] This may have resulted in lower formate FE% and higher $H_2$ FE% in the nano-Bi samples during electrocatalytic $CO_2$ reduction compared to the respective micro-Bi samples.

The surface hydrophilicities of micro-Bi and nano-Bi samples were studied by measuring the contact angles of water droplets on their surfaces (Figure 6). Photographs of water droplets on four sample surfaces clearly show an increase in the surface affinity of bismuth films for water (lower water contact angles) upon the formation of nanoscale roughness on the surface. The water contact angle on each sample surface was measured three times, and averaged values are displayed in Figure 6e. The average water contact angles of micro-Bi-180s and micro-Bi-300s were 111.1° and 119.8°, and they decreased to 58.3° and 66.7° as the additional nanostructures formed on the bismuth films with similar thicknesses (nano-Bi-180s and nano-Bi-300s).

The surfaces of the four bismuth films (micro-Bi-180s, micro-Bi-300s, nano-Bi-180s, and nano-Bi-300s) were analyzed by means of X-ray photoelectron spectroscopy (XPS) (Figure 7). Figure 7a,b shows the Bi 4f and C 1s core-level XPS spectra of the four films. The binding-energy position of Bi $4f_{7/2}$ core levels varied in energy from 158.84 to 159.34 eV and can be tentatively assigned to oxidized bismuth atoms. It is likely that the surface of the bismuth films underwent oxidation upon exposure to ambient air before XPS measurements. The oxidized bismuth atoms on the sample surfaces seemed to


https://doi.org/10.1021/acsomega.4c09642
ACS Omega 2024, 9, 48855−48866

**Table 2. Summary of Faradaic Efficiency (FE%) Values of Nano-Bi-180s and Nano-Bi-300s.**[a]

| nano-Bi-180s | | | | |
|---|---|---|---|---|
| V vs RHE | FE% for formate | FE% for $CH_4$ | FE% for CO | FE% for $H_2$ |
| −0.776 | 89.99 | 0 | 2.81 | 9.95 |
| −0.976 | 73.26 | 0.45 | 2.1 | 25.77 |
| −1.176 | 72.73 | 0.75 | 1.78 | 30.31 |
| −1.376 | 42.91 | 0.56 | 0.70 | 59.60 |
| nano-Bi-300s | | | | |
| V vs RHE | FE% for formate | FE% for $CH_4$ | FE% for CO | FE% for $H_2$ |
| −0.776 | 89.72 | 0 | 2.76 | 9.25 |
| −0.976 | 80.34 | 0 | 2.97 | 17.59 |
| −1.176 | 70.41 | 0 | 1.73 | 30.7 |
| −1.376 | 43.54 | 0.24 | 0.79 | 57.45 |

[a]Summary of Faradaic efficiency (FE%) values for formate, $CH_4$, CO, and $H_2$ with two nano-Bi samples determined by 30 min of chronoamperometry under a constant $CO_2$ flow at four different potential bias conditions (−0.776, −0.976, −1.176, and −1.376 V vs. RHE)

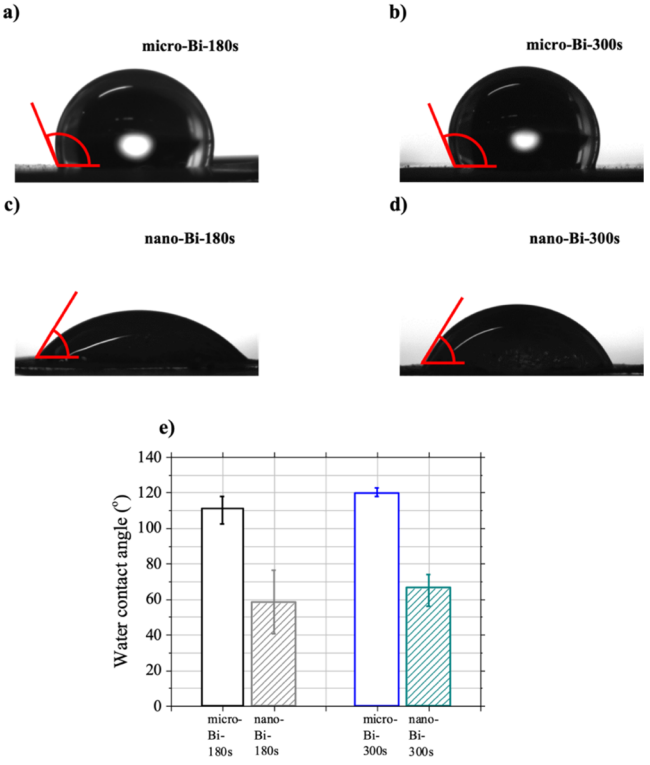


**Figure 6.** Results of water contact angle measurements. Photographs of water droplets on the surface of (a) micro-Bi-180s, (b) micro-Bi-300s, (c) nano-Bi-180s, and (d) nano-Bi-300s. (e) Comparison of averaged values of water contact angles for the surfaces of micro-Bi-180s, nano-Bi-180s, micro-Bi-300s, and nano-Bi-300s.

undergo reduction at the beginning of electrocatalytic $CO_2$ reduction (<approximately 1 min) when the bismuth films were biased at reductive (negative) potentials. After this short reduction period, electrocatalytic $CO_2$ reduction proceeded on bismuth films with atoms in lower oxidation states. The Bi 4f core-level spectra taken before the electrocatalytic $CO_2$ experiments did not provide precise information to determine the exact oxidation states of bismuth films responsible for the electrocatalytic behavior toward $CO_2$ reduction, particularly in terms of the FE% obtained from 30 min of $CO_2$ reduction. This can be addressed by operando analysis, such as operando X-ray absorption spectroscopy, which presents an interesting avenue for further scientific exploration.

Along with Bi signals, Cu-related XPS peaks (Cu 2p) were also observed in some samples (micro-Bi-180s, nano-Bi-180s, and nano-Bi-300s) (Figure S5), indicating that the underlying Cu films were not completely covered by the electrodeposited Bi films. Although the extent of exposed Cu atoms was minimal, as indicated by the very low intensity of Cu 2p peaks relative to Bi 4f peaks, the potential role of these Cu atoms during electrocatalytic $CO_2$ reduction cannot be completely excluded. However, variations in Cu 2p peak intensity across the samples did not correlate with their electrocatalytic behaviors, particularly the lower formate FE% and higher $H_2$ FE% observed in nano-Bi samples compared to micro-Bi samples. This suggested that the extent of exposed Cu atoms was not a major factor determining the differences in product selectivity between nano-Bi and micro-Bi samples. In addition, we mention that no Ti-related XPS peaks were observed in nano-Bi samples, allowing us to exclude any potential influence of Ti foil, which served as an underlay for the nano-Bi samples, on their electrocatalytic behaviors (Figure S5).

The C 1s core-level XPS spectra of the four samples at 285.64 eV can be attributed to adventitious carbon formed during electrodeposition of bismuth films (Figure 7b). These carbon species likely originated primarily from glycidol added to the electrodeposition solution as an electrolyte. The C 1s peak shapes and the binding-energy positions of the four samples were almost identical (Figure 7b and Figure S6). However, the nano-Bi samples had lower C 1s peak intensities compared with the respective micro-Bi samples (Figure 7b). Figure 7c shows the relative peak intensities of C 1s to Bi 4f core-level spectra of the four samples. These results imply that lower carbon content on the surface of the bismuth films of the nano-Bi samples compared with the respective micro-Bi samples also contributed to an increase in surface affinity toward water on the bismuth films of the nano-Bi samples compared to that of the micro-Bi samples.

Additionally, electrochemical impedance spectroscopy (EIS) analysis was performed on micro-Bi-180s and micro-Bi-300s and nano-Bi-180s and nano-Bi-300s samples to investigate whether the additional nanostructuring and reduced carbon content on the surface of nano-Bi samples alter their charge transfer properties compared to those of micro-Bi samples (Figure S7). The Nyquist plots from EIS analysis of all four samples exhibited similar semicircle shapes. The diameters of these semicircles, interpreted through the Randles circuit model, corresponded to the charge transfer resistance ($R_{ct}$) from the surface to electrolyte. The EIS results, along with Nyquist plots, revealed that the micro-Bi and nano-Bi samples with comparable Bi layer thicknesses exhibited very similar $R_{ct}$ values.

Our experimental results are summarized schematically in Figure 8. $CO_2$ and water molecules competed with each other for reductive reactions on the surface of negatively biased bismuth electrodes during electrocatalytic $CO_2$ reduction under aqueous solutions (Figure 8). The existence of nanoscale roughness and lower surface-carbon content on the bismuth surfaces can both lead to an increase in the bismuth surface affinity toward water molecules (Figure 8). As the affinity of the bismuth surface toward water increased, reductive reactions of water and $CO_2$ were favored and less-


https://doi.org/10.1021/acsomega.4c09642
ACS Omega 2024, 9, 48855−48866

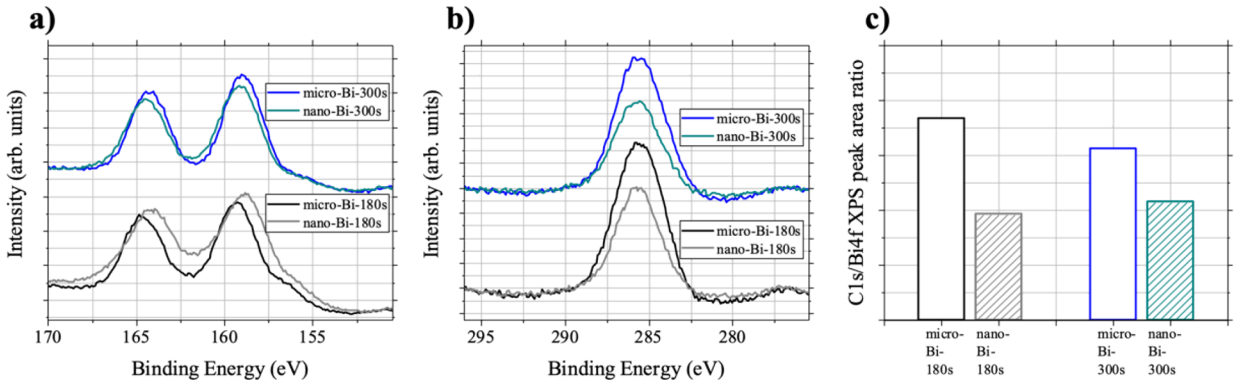


**Figure 7.** Results of XPS analysis. (a) Bi 4f and (b) C 1s core-level XPS spectra of micro-Bi-180s, nano-Bi-180s, micro-Bi-300s, and nano-Bi-300s. (c) Intensity ratios between C 1s and Bi 4f core-level XPS spectra of four samples (micro-Bi-180s, nano-Bi-180s, micro-Bi-300s, and nano-Bi-300s).

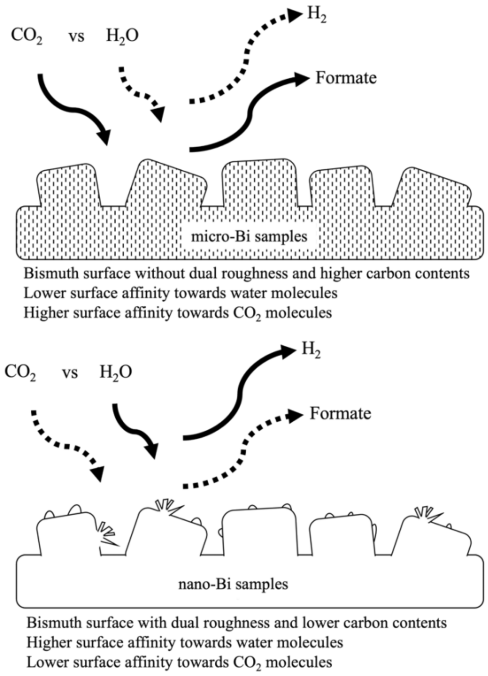


**Figure 8.** Schematic summary of the experimental results with micro- and nano-Bi samples.

favored, respectively, resulting in an increase in the FE% of $H_2$ and a decrease in formate FE%.

It is noteworthy that the cathodic currents remained relatively constant for all micro-Bi and nano-Bi samples during the long-term CO2RR operation (10 h) (S11). The formate Faradaic efficiency (FE%) for each sample also remained comparable to the values observed in the short-term operation (30 min). However, a slight decrease in formate FE% was observed for all samples as the operation time extended from 30 min to 10 h (S11). This reduction is likely due to the formation of additional nanostructures on the sample surfaces during the prolonged operation. For example, the formate FE% of micro-Bi-300s decreased from 93.38% at 30 min to 90.03% after 10 h of operation. The formation of nanostructures and the increase in hydrophilicity after long-term operation were confirmed by additional SEM and contact angle measurements conducted after 10 h (S11). These findings suggest that changes in the surface structure and hydrophilicity occur during extended CO2RR operation, which can influence the product selectivity. This warrants further investigation.

## 3. CONCLUSIONS

The electrocatalytic behavior of electrodeposited bismuth films toward $CO_2$ reduction under aqueous solutions was investigated. Two types of bismuth films were prepared by depositing bismuth films on copper foil (micro-Bi) and electroplated copper films (nano-Bi). The surfaces of the micro-Bi samples consisted of granular particles (400−800 nm) while those of the nano-Bi consisted of granular particles (400−800 nm) decorated with smaller nanostructures a few tens of nanometers in diameter, producing nanoscale roughness on the surface of the bismuth films of the nano-Bi. Formate and $H_2$ were the major products of electrocatalytic $CO_2$ reduction in all bismuth films studied (micro-Bi and nano-Bi samples). Decreases (increases) in the FE% of formate upon varying the potential bias conditions are always accompanied by increases (decreases) in the FE% of $H_2$, indicating that $CO_2$ and $H_2$ molecules competed with each other for reductive reactions on bismuth surfaces under aqueous conditions.

The surface of bismuth films on the nano-Bi samples exhibited higher surface affinity toward water molecules compared with those of the micro-Bi samples due to nanoscale roughness and lower surface-carbon content. This preference for water reduction on the surface of the nano-Bi, compared with the micro-Bi under the same potential bias condition, led to a lower formate FE% and higher $H_2$ FE% in the nano-Bi compared to the respective micro-Bi samples. These experimental observations imply that the product selectivity of electrocatalytic $CO_2$ reduction in aqueous solution can be altered by controlling the surface hydrophilicity (surface roughness and the type and amount of surface carbon) of bismuth electrodes.

## 4. MATERIALS AND METHODS

**4.1. Sample Preparation (Nano-Bi-180s, Nano-Bi-300s, and Nano-Bi-1800s).** Bismuth(III) chloride ($BiCl_3$, ≥ 98%), hydrochloric acid solution (HCl, ≥ 37%), and glycidol ($C_3H_6O_2$, ≥ 96%) were purchased from Sigma-Aldrich. The solution for bismuth electrodeposition was prepared by dissolving 0.316 g of bismuth(III) chloride in a 30 mL solution containing 3 mL of hydrochloric acid (HCl) solution, 1 mL of glycidol, and 26 mL of distilled water. The electrodeposition solution was agitated for 1 h at room temperature prior to the electrodeposition of bismuth.

Bismuth was electrodeposited on the surface of copper (Cu) foil (≥99.8%, Sigma-Aldrich) using a three-electrode electro-


https://doi.org/10.1021/acsomega.4c09642
ACS Omega 2024, 9, 48855−48866

chemical cell. The surface of the copper foil was sequentially immersed in acetone, ethanol, and deionized (DI) water, and the surface was gently wiped with disposable wipes. The cleaned foil was then annealed at 300 °C for 2 h in ambient conditions by using a box-type furnace prior to the electrodeposition of Bi.

The pretreated copper foil was installed in the three-electrode apparatus, which was filled with an electrodeposition solution of $BiCl_3$, HCl, glycidol, and DI water. An Ag/AgCl electrode filled with saturated KCl solution was used as reference electrode, and the copper foil (0.5 × 2 $cm^2$) and platinum (Pt) plate (2 × 2 $cm^2$) were used as working and counter electrodes, respectively. A platinum plate was almost completely immersed in the solution, and the lower half of the copper foil (0.5 × 1 $cm^2$) was immersed in the solution (bismuth deposition area: 0.5 × 1 $cm^2$). The foil was negatively biased (−0.2 V) with respect to the reference electrode, and the electrodeposition proceeded under a constant voltage condition (the copper foil was biased at −0.2 V vs Ag/AgCl) using a potentiostat; Auto lab PGSTAT302N, Metrohm AG, Swiss). The deposition currents were maintained at a stable level (−50 mA) throughout 180, 300, and 1800 s of bismuth electrodeposition on copper foil. After the designated deposition time, the applied voltage was reduced to zero, and the bismuth-deposited copper foil was extracted from the electrochemical reactor. Finally, the surface of the resulting sample surface was rinsed with distilled water in preparation for the electrocatalytic reduction of $CO_2$. Three samples with different amounts of deposited bismuth were prepared and labeled micro-Bi-180s, micro-Bi-300s, and micro-Bi-1800s, with the numbers indicating the electrodeposition time in seconds.

**4.2. Sample Preparation (Nano-Bi-180s and Nano-Bi-300s).** Electrodeposition of bismuth was also performed on electroless plated copper films on a titanium foil (eCu/Ti). The titanium foil (≥99%, thickness of 0.1 mm) was purchased from Koralco (South Korea). The foil was immersed in a 0.1% hydrofluoric acid (HF) solution for 10 min for chemical etching, and the etched foil was rinsed with distilled water. The copper film was deposited on the etched titanium foil surface using an electroless copper-plating method (MSMIS-80) purchased from MSC Co. (South Korea). Copper film was deposited on the surface of etched titanium foil (lateral size of 0.5 cm × 2 cm) by immersing the titanium foil in the solution (at 60 °C) for 1 h. The foil was then rinsed with distilled water and subjected to annealing at 300 °C for 2 h under ambient conditions by using a box-type furnace. The resulting eCu/Ti foil was used as a substrate for the electrodeposition of bismuth to prepare nano-Bi samples. All bismuth electrodeposition procedures were identical to those used to prepare the micro-Bi samples (section 4.1). Two different nano-Bi samples, nano-Bi-180s and nano-Bi-300s, were prepared by depositing bismuth for 180 and 300 s, respectively, on the electroless plated copper films.

**4.3. Sample Characterization (SEM-Topological Image, SEM-Cross-sectional Image, SEM-EDS, XRD, XPS, Water Contact Angle).** Geometrical and crystal structures of micro-Bi and nano-Bi samples were analyzed by SEM and XRD, respectively. Topological and cross-sectional SEM images were obtained by using a thermal field-emission electron microscope (JSM-7100F, JEOL, Japan). SEM-EDS images were also obtained by using the same electron microscope. XRD patterns of samples were obtained with an X-ray diffractometer (Rigaku Ultima IV, Rigaku, Japan) using Cu K-alpha radiation (8.04 keV). The surface of each sample was analyzed by means of XPS at room temperature under ultrahigh-vacuum conditions (a base pressure of approximately 3.0 × $10^{-10}$ Torr). X-rays were provided by a Mg K-alpha source (1.254 keV), and photoelectrons from the sample surface were detected by a concentric hemispherical analyzer (PHOIBOS 150 1D-DLD, SPECS, Germany). The contact angle of water droplets (3 μL) on each sample surface was determined by using an optical tensiometer (Theta Lite, Biolin Scientific, Sweden) to examine the hydrophilicity of each sample surface.

**4.4. Electrocatalytic $CO_2$ Reduction (LSV, Current Density vs Time, Product Analysis—GC and NMR).** Electrocatalytic $CO_2$ reduction was performed with micro-Bi and nano-Bi samples using a three-electrode H-type cell with a total volume of 100 mL. A schematic of the reactor can be found in Scheme S1. The cell consisted of two compartments (working- and counter-electrode compartments) connected through an N115 Nafion membrane. The top parts of both compartments were sealed with poly(tetrafluoroethylene) (PTFE) lids, each of which had ports for the installation of electrodes and gas lines. Bismuth-deposited samples were installed in the working-electrode compartment of the H-type cell together with a reference electrode (a Ag/AgCl electrode filled with a saturated AgCl solution). A platinum plate (2 × 2 $cm^2$) was used as counter-electrode and installed in the counter-electrode compartment of the H-type cell. Each compartment of the H-type cell was filled with 40 mL of the electrolyte solution (0.5 M of $KHCO_3$). Both the bismuth films (0.5 × 1 $cm^2$) and platinum plate (2 × 2 $cm^2$) were almost completely immersed in the electrolyte. Two additional gas lines (in and out) were installed in the working-electrode compartment through the ports of the PTFE lid. The electrolyte solution in the working electrode was bubbled by the desired gas ($CO_2$ or $N_2$) using the gas-in line, and the flow rate of the gas was controlled by a mass flow controller (MFC, VIC-D220, MKP, South Korea).

Electrocatalytic activities of micro-Bi and nano-Bi samples toward $CO_2$ reduction were investigated by means of LSV and chronoamperometry. An electrolyte solution was presaturated by $CO_2$ gas flowing at a constant rate of 20 sccm for 1 h prior to the taking of electrochemical measurements, and $CO_2$ gas was constantly flowed at 20 sccm into the electrolyte while measurements were taken. The voltage applied to the working electrode (bismuth-deposited samples) during LSV measurements ranged from −0.8 to −2.0 V with respect to the reference electrode at a constant scan rate (0.1 V/s). The values of the potential applied on the working electrode were later calculated (in volts) with respect to reversible hydrogen electrode (V vs RHE) using the equation $E_{(RHE)} = E_{Ag/AgCl} + 0.059\ pH + E^{\circ}_{Ag/AgCl}$. For comparison, the LSV measurement was also performed with each bismuth-deposited sample under a constant $N_2$ gas flow of 20 sccm.

Chronoamperometry measurements were performed by measuring the current flow from the working electrode to the counter-electrode, while the working electrode was biased at a fixed potential with respect to the reference electrode under the constant $CO_2$ flow (20 sccm). The measurements were carried out under four different potential biases (−0.776, −0.976, −1.176, and −1.376 V vs RHE) for 30 min. Reaction products in gas phase were analyzed by an online GC (6890N, Agilent Technologies, USA) equipped with a six-way gas-


https://doi.org/10.1021/acsomega.4c09642
ACS Omega 2024, 9, 48855−48866

sampling valve, thermal conductivity detector (TCD), and flame ionization detector (FID). Agilent HP-Plot Q (19095P-QO4, Agilent Technologies, USA) was used as a GC column, and high-purity $N_2$ gas was used as a carrier gas. The calibration curves for the five gas molecules ($CH_4$, CO, $C_2H_4$, $C_2H_6$, and $H_2$) were obtained by using the respective standard gases (1% $CH_4$, 1% CO, 1% $C_2H_4$, 1% $C_2H_6$, and 3% $H_2$). Products of the $CO_2$ reduction products in the liquid phase were analyzed by an NMR apparatus (Unity INOVA500, Varian, USA). After 30 min of chronoamperometry experiments, 700 $\mu$L of aliquot of the electrolyte was taken out of the working electrode compartment of the H-type cell. The aliquot was mixed with 35 $\mu$L of $D_2O$ containing 10 mM dimethyl sulfoxide (DMSO) and 50 mM phenol as internal standards. The calibration curve for formate NMR signal to formate concentration conversion was determined based on the results of the NMR analysis of the standard formate solutions (10, 30, 50, and 100 mM).

## ■ ASSOCIATED CONTENT

### Supporting Information

The Supporting Information is available free of charge at https://pubs.acs.org/doi/10.1021/acsomega.4c09642.

Results of SEM-EDS mapping analysis on micro-Bi-180s, micro-Bi-300s, and micro-Bi-1800s samples (S2, Figure S1); details of depth estimation for XRD analysis (S3); results of LSV measurements with micro-Bi samples under $N_2$ and $CO_2$ flow, including comparisons of LSV curves for micro-Bi-180s and micro-Bi-300s under $N_2$ and $CO_2$ flow (S4, Figure S2); detailed information on the FE% calculation (S5); results of SEM-EDS mapping analysis on nano-Bi-180s and nano-Bi-300s samples (S6, Figure S3); LSV curves obtained under $N_2$ and $CO_2$ flow conditions with nano-Bi-180s and nano-Bi-300s (S7, Figure S4); Cu 2p core-level XPS spectra of four samples (micro-Bi-180s, nano-Bi-180s, micro-Bi-300s, and nano-Bi-300) after intensity normalization with respect to the respective Bi 4f core-level XPS spectra and Ti 2p3/2 core-level XPS spectra of nano-Bi samples (S8, Figure S5); Bi 4f (left) and C 1s (right) core-level XPS spectra of four samples (micro-Bi-180s, nano-Bi-180s, micro-Bi-300s, and nano-Bi-300) after intensity normalization with respect to the respective C 1s core-level XPS spectra (S9, Figure S6); Nyquist plots from EIS analysis of micro-Bi-180s and micro-Bi-300s and nano-Bi-180s and nano-Bi-300s (S10, Figure S7); current density as a function of reaction time (10 h) at −0.776 V of micro-Bi-180s, micro-Bi-300s, and micro-Bi-1800s and nano-Bi-180s and nano-Bi-300s (S11, Figure S8); table for formate FE% for short-term and long-term CO2RR (−0.776) (S11, Table S1); results of topological SEM and the water contact angle analyses of micro-Bi-300s after 10 h of CO2RR (S11, Figure S9); schematic of experimental setup for electrocatalytic $CO_2$ reduction (S12, Scheme S1) (PDF)

## ■ AUTHOR INFORMATION


### Corresponding Authors

**Young Dok Kim** − *Department of Chemistry, Sungkyunkwan University, Suwon 16419, Republic of Korea;* orcid.org/0000-0003-1138-5455; Phone: (+82) 31-299-4564; Email: ydkim91@skku.edu

**Hyun Ook Seo** − *Department of Chemistry and Energy Engineering, Sangmyung University, Seoul 03016, Republic of Korea;* orcid.org/0000-0002-8957-171X; Phone: (+82) 2-2287-6105; Email: hyun.ook.seo@smu.ac.kr

### Authors

**Yujing Ji** − *Department of Chemistry, Sungkyunkwan University, Suwon 16419, Republic of Korea*

**Jichuang Wu** − *Department of Chemistry, Sungkyunkwan University, Suwon 16419, Republic of Korea;* orcid.org/0009-0002-7504-8562

**Ha Eun Lee** − *Department of Chemistry and Energy Engineering, Sangmyung University, Seoul 03016, Republic of Korea*

**Yongsu An** − *Department of Chemistry, Sungkyunkwan University, Suwon 16419, Republic of Korea*

**Duk-Young Jung** − *Department of Chemistry, Sungkyunkwan University, Suwon 16419, Republic of Korea;* orcid.org/0000-0003-3152-6382

**Chan Woo Lee** − *Department of Chemistry, Kookmin University, Seoul 02707, Republic of Korea;* orcid.org/0000-0001-8370-1985

Complete contact information is available at: https://pubs.acs.org/10.1021/acsomega.4c09642


### Author Contributions

Y.J.: methodology, investigation, visualization. J.W.: methodology, investigation. H.E.L.: methodology, investigation. Y.A.: methodology. D.-Y.J.: resources, funding acquisition. C.W.L.: resources, funding acquisition. Y.D. Kim: resources, conceptualization, validation, supervision, funding acquisition H.O.S.: resources, conceptualization, validation, supervision, data curation, writing (original draft preparation), writing (reviewing and editing), funding acquisition.


### Funding

This work was supported by the National Research Foundation of Korea (NRF) grant funded by the Korea government (MSIT) (No. 2021R1F1A1045539) (No. 2022R1A4A1019296) and by the Graduate School of Green Restoration specialization of Korea Environmental Industry & Technology Institute (KEITI) funded by the Ministry of Environment (MOE).


### Notes

The authors declare no competing financial interest.

## ■ REFERENCES


(1) Friedlingstein, P.; O'sullivan, M.; Jones, M. W.; Andrew, R. M.; Gregor, L.; Hauck, J.; Le Quéré, C.; Luijkx, I. T.; Olsen, A.; Peters, G. P.; et al. Global carbon budget 2022. *Earth Syst. Sci. Data* **2022**, *14*, 4811−4900.

(2) López, L.; Dessì, P.; Cabrera-Codony, A.; Rocha-Melogno, L.; Kraakman, B.; Naddeo, V.; Balaguer, M.; Puig, S. $CO_2$ in indoor environments: From environmental and health risk to potential renewable carbon source. *Sci. Total Environ.* **2023**, *856*, No. 159088.

(3) Groll, M. Can climate change be avoided? Vision of a hydrogen-electricity energy economy. *Energy* **2023**, *264*, No. 126029.

(4) Rehman, A.; Alam, M. M.; Ozturk, I.; Alvarado, R.; Murshed, M.; Işık, C.; Ma, H. Globalization and renewable energy use: how are they contributing to upsurge the $CO_2$ emissions? A global perspective. *Environ. Sci. Pollut. Res.* **2023**, *30* (4), 9699−9712.

(5) Andrew, R. M. A comparison of estimates of global carbon dioxide emissions from fossil carbon sources. *Earth System Sci. Data* **2020**, *12* (2), 1437−1465.

(6) Bekun, F. V. Mitigating emissions in India: accounting for the role of real income, renewable energy consumption and investment in energy. *Int. J. Energy Econ. Policy* **2022**, *12*, 188.
(7) Martins, T.; Barreto, A. C.; Souza, F. M.; Souza, A. M. Fossil fuels consumption and carbon dioxide emissions in G7 countries: Empirical evidence from ARDL bounds testing approach. *Environ. Pollut.* **2021**, *291*, No. 118093.
(8) Yong, J. C.; Rahman, M.; Asli, R. A. Renewable energy: A brief review. *AIP Conf. Proc.* **2023**, *2643*, No. 030028.
(9) Jeong, M.-G.; Kim, S. Y.; Kim, D. H.; Han, S. W.; Kim, I. H.; Lee, M.; Hwang, Y. K.; Kim, Y. D. High-performing and durable MgO/Ni catalysts via atomic layer deposition for $CO_2$ reforming of methane (CRM). *APPL CATAL A-GEN* **2016**, *515*, 45−50.
(10) Kim, D. H.; Seo, H. O.; Jeong, M.-G.; Kim, Y. D. Reactivity and stability of Ni nanoparticles supported by mesoporous $SiO_2$ and $TiO_2/SiO_2$ for $CO_2$ reforming of $CH_4$. *Catal. Lett.* **2014**, *144*, 56−61.
(11) Cao, Y.; He, X.; Wang, N.; Li, H. R.; He, L. N. Photochemical and electrochemical carbon dioxide utilization with organic compounds. *Chin. J. Chem.* **2018**, *36* (7), 644−659.
(12) Bhattacharjee, S.; Rahaman, M.; Andrei, V.; Miller, M.; Rodríguez-Jiménez, S.; Lam, E.; Pornrungroj, C.; Reisner, E. Photoelectrochemical $CO_2$-to-fuel conversion with simultaneous plastic reforming. *Nat. Chem.* **2023**, *2* (2), 182−192.
(13) Raza, S.; Orooji, Y.; Ghasali, E.; Hayat, A.; Karimi-Maleh, H.; Lin, H. Engineering approaches for $CO_2$ converting to biomass coupled with nanobiomaterials as biomediated towards circular bioeconomy. *J. CO2 Util.* **2023**, *67*, No. 102295.
(14) Liu, Z.; Wang, K.; Chen, Y.; Tan, T.; Nielsen, J. Third-generation biorefineries as the means to produce fuels and chemicals from $CO_2$. *Nat. Catal.* **2020**, *3* (3), 274−288.
(15) Thulluru, L. P.; Ghangrekar, M. M.; Chowdhury, S. Progress and perspectives on microbial electrosynthesis for valorisation of $CO_2$ into value-added products. *J. Environ. Manage.* **2023**, *332*, No. 117323.
(16) Kas, R.; Yang, K.; Bohra, D.; Kortlever, R.; Burdyny, T.; Smith, W. A. Electrochemical $CO_2$ reduction on nanostructured metal electrodes: fact or defect? *Chem. Sci.* **2020**, *11* (7), 1738−1749.
(17) Farooqi, S. A.; Farooqi, A. S.; Sajjad, S.; Yan, C.; Victor, A. B. Electrochemical reduction of carbon dioxide into valuable chemicals: A review. *Environ. Chem. Lett.* **2023**, *21*, 1515−1553.
(18) Seo, H.; Hatton, T. A. Electrochemical direct air capture of $CO_2$ using neutral red as reversible redox-active material. *Nat. Commun.* **2023**, *14* (1), 313.
(19) Ewis, D.; Arsalan, M.; Khaled, M.; Pant, D.; Ba-Abbad, M. M.; Amhamed, A.; El-Naas, M. H. Electrochemical reduction of $CO_2$ into formate/formic acid: A review of cell design and operation. *Sep. Purif. Technol.* **2023**, *316*, No. 123811.
(20) Fernández-Caso, K.; Díaz-Sainz, G.; Alvarez-Guerra, M.; Irabien, A. Electroreduction of $CO_2$: advances in the continuous production of formic acid and formate. *ACS Energy Lett.* **2023**, *8* (4), 1992−2024.
(21) Zhai, S.; Jiang, S.; Liu, C.; Li, Z.; Yu, T.; Sun, L.; Ren, G.; Deng, W. Liquid sunshine: formic acid. *J. Phys. Chem. Lett.* **2022**, *13* (36), 8586−8600.
(22) Jouny, M.; Luc, W.; Jiao, F. General techno-economic analysis of $CO_2$ electrolysis systems. *Ind. Eng. Chem. Res.* **2018**, *57* (6), 2165−2177.
(23) Spurgeon, J. M.; Kumar, B. A comparative technoeconomic analysis of pathways for commercial electrochemical $CO_2$ reduction to liquid products. *Energy Environ. Sci.* **2018**, *11* (6), 1536−1551.
(24) Joó, F. Breakthroughs in Hydrogen Storage—Formic Acid as a Sustainable Storage Material for Hydrogen. *ChemSusChem* **2008**, *1* (10), 805−808.
(25) Calabrese, M.; Russo, D.; di Benedetto, A.; Marotta, R.; Andreozzi, R. Formate/bicarbonate interconversion for safe hydrogen storage: A review. *Renew. Sust. Energy Rev.* **2023**, *173*, No. 113102.
(26) Grubel, K.; Jeong, H.; Yoon, C. W.; Autrey, T. Challenges and opportunities for using formate to store, transport, and use hydrogen. *J. Energy Chem.* **2020**, *41*, 216−224.
(27) Zhang, W.; Hu, Y.; Ma, L.; Zhu, G.; Wang, Y.; Xue, X.; Chen, R.; Yang, S.; Jin, Z. Progress and perspective of electrocatalytic $CO_2$ reduction for renewable carbonaceous fuels and chemicals. *Adv. Sci.* **2018**, *5* (1), 1700275.
(28) Garg, S.; Li, M.; Weber, A. Z.; Ge, L.; Li, L.; Rudolph, V.; Wang, G.; Rufford, T. E. Advances and challenges in electrochemical $CO_2$ reduction processes: an engineering and design perspective looking beyond new catalyst materials. *J. Mater. Chem. A* **2020**, *8* (4), 1511−1544.
(29) Saha, P.; Amanullah, S.; Dey, A. Selectivity in electrochemical $CO_2$ reduction. *Acc. Chem. Res.* **2022**, *55* (2), 134−144.
(30) Wulan, B.; Cao, X.; Tan, D.; Shu, X.; Ma, J.; Hou, S.; Zhang, J. Atomic Bridging of Sn Single Atom with Nitrogen and Oxygen Atoms for the Selective Electrocatalytic Reduction of $CO_2$. *CCS Chem.* **2023**, 2415−2425.
(31) Zhang, S.; Kang, P.; Meyer, T. J. Nanostructured tin catalysts for selective electrochemical reduction of carbon dioxide to formate. *J. Am. Chem. Soc.* **2014**, *136* (5), 1734−1737.
(32) Yang, Z.; Oropeza, F. E.; Zhang, K. H. L. P-block metal-based (Sn, In, Bi, Pb) electrocatalysts for selective reduction of $CO_2$ to formate. *APL Mater.* **2020**, *8* (6), No. 060901.
(33) Han, N.; Ding, P.; He, L.; Li, Y.; Li, Y. Promises of main group metal−based nanostructured materials for electrochemical $CO_2$ reduction to formate. *Adv. Energy Mater.* **2020**, *10* (11), 1902338.
(34) Chen, Z.; Wang, N.; Yao, S.; Liu, L. The flaky Cd film on Cu plate substrate: An active and efficient electrode for electrochemical reduction of $CO_2$ to formate. *J. CO2 Util.* **2017**, *22*, 191−196.
(35) Yang, W.; Chen, S.; Ren, W.; Zhao, Y.; Chen, X.; Jia, C.; Liu, J.; Zhao, C. Nanostructured amalgams with tuneable silver−mercury bonding sites for selective electroreduction of carbon dioxide into formate and carbon monoxide. *J. Mater. Chem. A* **2019**, *7* (26), 15907−15912.
(36) Cheng, Q.; Huang, M.; Xiao, L.; Mou, S.; Zhao, X.; Xie, Y.; Jiang, G.; Jiang, X.; Dong, F. Unraveling the Influence of Oxygen Vacancy Concentration on Electrocatalytic $CO_2$ Reduction to Formate over Indium Oxide Catalysts. *ACS Catal.* **2023**, *13* (6), 4021−4029.
(37) Wulan, B.; Cao, X.; Tan, D.; Ma, J.; Zhang, J. To Stabilize Oxygen on $In/In_2O_3$ Heterostructure via Joule Heating for Efficient Electrocatalytic $CO_2$ Reduction. *Adv. Funct. Mater.* **2023**, *33* (1), 2209114.
(38) Cao, C.; Ma, D. D.; Jia, J.; Xu, Q.; Wu, X. T.; Zhu, Q. L. Divergent paths, same goal: a pair-electrosynthesis tactic for cost-efficient and exclusive formate production by metal−organic-framework-derived 2D electrocatalysts. *Adv. Mater.* **2021**, *33* (25), 2008631.
(39) Ma, D.-D.; Han, S.-G.; Zhou, S.-H.; Wei, W.-B.; Li, X.; Chen, B.; Wu, X.-T.; Zhu, Q.-L. Molecularly dispersed heterogenized metallomacrocycles: molecular structure sensitivity of $CO_2$ electrolysis, CCS. *CCS Chem.* **2023**, *5* (8), 1827−1840.
(40) Yang, S.; Jiang, M.; Zhang, W.; Hu, Y.; Liang, J.; Wang, Y.; Tie, Z.; Jin, Z. In situ structure refactoring of bismuth nanoflowers for highly selective electrochemical reduction of $CO_2$ to formate. *Adv. Funct. Mater.* **2023**, *33* (37), 2301984.
(41) Li, Z.; Feng, Y.; Li, Y.; Chen, X.; Li, N.; He, W.; Liu, J. Fabrication of Bi/Sn bimetallic electrode for high-performance electrochemical reduction of carbon dioxide to formate. *Chem. Eng. J.* **2022**, *428*, No. 130901.
(42) Li, L.; Ma, D.-K.; Qi, F.; Chen, W.; Huang, S. Bi nanoparticles/$Bi_2O_3$ nanosheets with abundant grain boundaries for efficient electrocatalytic $CO_2$ reduction. *Electrochim. Acta* **2019**, *298*, 580−586.
(43) Lin, L.; He, X.; Zhang, X. G.; Ma, W.; Zhang, B.; Wei, D.; Xie, S.; Zhang, Q.; Yi, X.; Wang, Y. A nanocomposite of bismuth clusters and $Bi_2O_2CO_3$ sheets for highly efficient electrocatalytic reduction of $CO_2$ to formate. *Angew. Chem., Int. Ed.* **2023**, *135* (3), No. e202214959.
(44) Liang, X.-D.; Tian, N.; Hu, S.-N.; Zhou, Z.-Y.; Sun, S.-G. Recent advances of bismuth-based electrocatalysts for CO2 reduction:


https://doi.org/10.1021/acsomega.4c09642
*ACS Omega* 2024, 9, 48855−48866

Strategies, mechanism and applications. *Materials Reports: Energy* **2023**, *3* (2), No. 100191.
(45) Han, N.; Wang, Y.; Yang, H.; Deng, J.; Wu, J.; Li, Y.; Li, Y. Ultrathin bismuth nanosheets from in situ topotactic transformation for selective electrocatalytic $CO_2$ reduction to formate. *Nat. Commun.* **2018**, *9* (1), 1320.
(46) Deng, P.; Wang, H.; Qi, R.; Zhu, J.; Chen, S.; Yang, F.; Zhou, L.; Qi, K.; Liu, H.; Xia, B. Y. Bismuth oxides with enhanced bismuth−oxygen structure for efficient electrochemical reduction of carbon dioxide to formate. *ACS Catal.* **2020**, *10* (1), 743−750.
(47) Lamagni, P.; Miola, M.; Catalano, J.; Hvid, M. S.; Mamakhel, M. A. H.; Christensen, M.; Madsen, M. R.; Jeppesen, H. S.; Hu, X.; Daasbjerg, K.; Skrydstrup, T.; Lock, N. Restructuring metal−organic frameworks to nanoscale bismuth electrocatalysts for highly active and selective $CO_2$ reduction to formate. *Adv. Funct. Mater.* **2020**, *30* (16), No. 1910408.
(48) Zeng, G.; He, Y.; Ma, D. D.; Luo, S.; Zhou, S.; Cao, C.; Li, X.; Wu, X. T.; Liao, H. G.; Zhu, Q. L. Reconstruction of Ultrahigh-Aspect-Ratio Crystalline Bismuth−Organic Hybrid Nanobelts for Selective Electrocatalytic $CO_2$ Reduction to Formate. *Adv. Funct. Mater.* **2022**, *32* (30), 2201125.
(49) Liu, S.-Q.; Gao, M.-R.; Feng, R.-F.; Gong, L.; Zeng, H.; Luo, J.-L. Electronic delocalization of bismuth oxide induced by sulfur doping for efficient $CO_2$ electroreduction to formate. *ACS Catal.* **2021**, *11* (12), 7604−7612.
(50) Cao, X.; Tian, Y.; Ma, J.; Guo, W.; Cai, W.; Zhang, J. Strong p-d Orbital Hybridization on Bismuth Nanosheets for High Performing $CO_2$ Electroreduction. *Adv. Mater.* **2023**, *36*, No. 2309648.
(51) Nankya, R.; Xu, Y.; Elgazzar, A.; Zhu, P.; Wi, T. U.; Qiu, C.; Feng, Y.; Che, F.; Wang, H. Cobalt-Doped Bismuth Nanosheet Catalyst for Enhanced Electrochemical $CO_2$ Reduction to Electrolyte-Free Formic Acid. *Angew. Chem., Int. Ed.* **2024**, *63*, No. e202403671.
(52) Lv, W.; Bei, J.; Zhang, R.; Wang, W.; Kong, F.; Wang, L.; Wang, W. $Bi_2O_2CO_3$ nanosheets as electrocatalysts for selective reduction of CO2 to formate at low overpotential. *ACS omega* **2017**, *2* (6), 2561−2567.
(53) Hu, Y.; Liang, J.; Gu, Y.; Yang, S.; Zhang, W.; Tie, Z.; Ma, J.; Jin, Z. Sandwiched epitaxy growth of 2D single-crystalline hexagonal bismuthene nanoflakes for electrocatalytic $CO_2$ reduction. *Nano Lett.* **2023**, *23* (22), 10512−10521.
(54) Yang, F.; Elnabawy, A. O.; Schimmenti, R.; Song, P.; Wang, J.; Peng, Z.; Yao, S.; Deng, R.; Song, S.; Lin, Y.; Mavrikakis, M.; Xu, W. Bismuthene for highly efficient carbon dioxide electroreduction reaction. *Nat. Commun.* **2020**, *11* (1), 1088.
(55) Zhang, M.; Wei, W.; Zhou, S.; Ma, D.-D.; Cao, A.; Wu, X.-T.; Zhu, Q.-L. Engineering a conductive network of atomically thin bismuthene with rich defects enables $CO_2$ reduction to formate with industry-compatible current densities and stability. *Energy Environ. Sci.* **2021**, *14* (9), 4998−5008.
(56) Nolan, M. Adsorption of $CO_2$ on heterostructures of $Bi_2O_3$ nanocluster-modified $TiO_2$ and the role of reduction in promoting $CO_2$ activation. *ACS omega* **2018**, *3* (10), 13117−13128.
(57) Wang, M.; Wang, H.; Gu, Y.; Zhu, M.; Kumar, M.; Liang, J.; Tie, Z.; Ma, J.; Jin, Z. In Situ Generation of Flash Graphene Supported Spherical Bismuth Nanoparticles in Less than 200 ms for Highly Selective Carbon Dioxide Electroreduction. *ACS Materials Letters* **2024**, *6* (1), 100−108.
(58) Yang, S.; Wang, H.; Xiong, Y.; Zhu, M.; Sun, J.; Jiang, M.; Zhang, P.; Wei, J.; Xing, Y.; Tie, Z.; Jin, Z. Ultrafast Thermal Shock Synthesis and Porosity Engineering of 3D Hierarchical Cu−Bi Nanofoam Electrodes for Highly Selective Electrochemical $CO_2$ Reduction. *Nano Lett.* **2023**, *23* (22), 10140−10147.
(59) Park, E. J.; Kim, H. J.; Han, S. W.; Jeong, J. H.; Kim, I. H.; Seo, H. O.; Kim, Y. D. Assembly of PDMS/$SiO_2$-PTFE and activated carbon fibre as a liquid water−resistant gas sorbent structure. *Chem. Eng. J.* **2017**, *325*, 433−441.
(60) Park, E. J.; Seo, H. O.; Kim, Y. D. Influence of humidity on the removal of volatile organic compounds using solid surfaces. *Catal. Today* **2017**, *295*, 3−13.


https://doi.org/10.1021/acsomega.4c09642
*ACS Omega* 2024, 9, 48855−48866